Please cite this paper as

Chen Z and Zhu S (2022) Development of A Novel SMA-based Self-centering Precast Segmental Concrete Column. Structural Control and Health Monitoring. 29: e3099. https://doi.org/10.1002/stc.3099

Development of a novel SMA-based self-centering precast segmental concrete column

Zhi-Peng Chen[1], Songye Zhu[1,*]
[1] Department of Civil and Environmental Engineering, The Hong Kong Polytechnic University, Hong Kong, China
* Corresponding author: S. Zhu, Email: songye.zhu@polyu.edu.hk

ABSTRACT

This study proposes a novel shape memory alloy (SMA)-based self-centering (SC) precast segmental concrete column (PSCC). The entire structural system, called SSC-PSCC, can be constructed via off-site precasting followed by on-site assembly. By using connected SMA bolts and steel angles, wherein SMA and steel elements contribute to SC and energy dissipation (ED) capacities, respectively, SSC-PSCC is free from post-tensioned anchorage and wet joints, and the construction or repair process is considerably simplified. The behavior of SSC-PSCC was systematically studied through refined finite element models (FEMs) that were verified by good agreements with previous testing results. Cyclic behavior was simulated, and SSC-PSCC exhibits desirable SC and ED capacities. Compared with traditional post-tensioning (PT)-based SC-PSCC, SSC-PSCC has numerous advantages, including easy construction, quick repair and replacement of ED elements after earthquakes, and free from buckling observed in ED bars of traditional PT-based segmental columns. Furthermore, parametric studies were conducted to identify several crucial design parameters, such as prestrain in SMA bolts, axial load ratio, and segment reinforcement diameter. Design recommendations are provided on the basis of the results of the parametric studies.

Keywords: shape memory alloy, precast segmental concrete column, self-centering, hysteretic analysis, parametric study

1. INTRODUCTION

Precast segmental concrete columns (PSCCs) have recently elicited considerable interests in the field of bridge engineering and have been widely used in actual engineering projects to achieve accelerated bridge construction [1, 2]. Segmental bridge piers are typically prefabricated in factories and can minimize initial defects, environmental impact, and post-seismic residual displacements. Traditionally, precast segmental columns are limited in low seismicity areas due to a lack of knowledge regarding their seismic performance [3]. Several recent studies [4, 5] conducted meaningful tests and simulations regarding this issue, proving that well-designed segmental columns can fully meet seismic-resistant requirements.

In recently developed PSCCs, unbonded post-tensioning (PT) tendons and energy dissipation (ED) components have been widely used, wherein unbonded PT tendons are the core elements. Their seismic behavior has been investigated. For example, Hewes and Priestley [6] conducted pioneer studies. Theoretical and experimental studies have shown that segmental columns equipped with unbonded PT tendons can effectively restrain structural deformation under seismic loading and exhibit desirable self-centering (SC) capacity. Chang et al. [7] and Ou et al. [8] used mild steel bars (often referred to as ED bars) to solve the low ED capacity problem of the designs with only PT tendons. A flag-shaped hysteretic behavior was achieved, and the seismic resilience concept and

accelerated bridge construction were well connected. After the design framework of segmental bridge columns was determined, subsequent studies focused more on improving the efficiency of ED devices. Chou and Chen [9] demonstrated that using concrete-filled tubes could evidently increase the equivalent viscous damping ratio of segmental columns. Other energy dissipation devices, including external replaceable energy dissipaters [10], steel angles [11], and built-in elastomer pads [12], were also used. In addition to different types of ED devices, high-quality materials, such as high-performance steel [13] or ductile fiber-reinforced concrete [14], were also selected to achieve higher ductility, better energy dissipation, and higher strength for segmental columns. Apart from experimental studies, numerical studies through finite element models (FEMs) were correspondingly conducted. The 3D refined elements in Abaqus [15, 16] and the global fiber and node elements in OpenSEES [17, 18] demonstrated efficiency and accuracy in simulation studies.

Previous studies have shown that currently available SC-PSCC can achieve good seismic and SC performance; however, most designs are highly dependent on PT tendons. The requirements for anchorages and elasticity of tendons during operation pose additional difficulties and restraints to designs and applications, and the pouring of high-strength grout for anchoring ED bars also causes problems in post-seismic repair and replacement. An innovative strategy is to use shape memory alloys (SMAs) as an alternative solution [19, 20]. These high-performance alloys can recover their initial state due to heating (shape memory effect, SME) or unloading (superelastic effect). They have been recently used as promising SC elements in civil engineering structures [21, 22]. Superelastic SMA is typically preferred in civil engineering. Many researchers have used this alloy because of its typical flag-shaped hysteresis behavior, which offers desirable SC and moderate ED capacities [23, 24]. Moreover, the excellent corrosion resistance and high fatigue resistance of superelastic SMA make it favorable in considerable of life-cycle maintenance in civil infrastructure [25, 26]. To date, many types of SMA-based SC devices and dampers have been proposed, including SMA wires [27], SMA cables [28], SMA bolts [29], SMA angles [30], SMA U-shaped dampers [31], etc. They are used as connections [32], bracings [33], passive control devices [34] or dampers [35] in different types of structural systems. SMA devices exhibit an evident advantage of achieving SC behavior under large strain (i.e., over 8%) [26], helping simplify the configurations of corresponding structures and achieving complete precast fabrication.

In the current study, a novel SMA-based SC-PSCC (SSC-PSCC) design, which had not been investigated in the literature, was proposed. Its seismic performance was investigated through numerical studies. The column segments can be precast in a factory and connected completely with SMA and steel bolts. No post-pouring wet joints were necessary. Steel angles were used to enhance ED capacity, and the application of SMA bolts achieved good SC capacity in the segmental column. Refined FEMs were established on the basis of previous test results, and several parametric studies were conducted to explore the core parameters in the design.

2. CONFIGURATION OF SSC-PSCC

Figure 1 illustrates the configuration of SSC-PSCC. The primary parts of the column are the precast concrete segments. These hollow concrete segments are precast in factories and then assembled in the field. Several holes remain at the corners of the segments to place connection bolts. The middle part of the corners is caverned out to facilitate the bolt placement. The segments are connected by SMA and steel bolts. In a desirable design, the gap opening and closing should be

concentrated at the bottom of the column, particularly the base segment. To balance SC capacity and monetary cost, SMA bolts are used only in the bottom parts while the other segments are connected by steel bolts. Steel flat slabs are placed between the bottom two segments, enhancing the gap opening force and guaranteeing that the gap opening is concentrated at the bottom of the entire column. Moreover, several steel angles are placed at the bottom of the column, enhancing the ED capacity of SSC-PSCC. In this novel SSC-PSCC, all the connections utilize bolts; thus, the column is completely free from PT anchorage or post-pouring. Consequently, construction speed can be considerably accelerated. Moreover, all the elements, including the SMA bolts, steel bolts, and ED angles, can be easily repaired and replaced after an earthquake. Furthermore, concrete segments can be free from damage or replacement, largely reducing the workload and monetary loss of post-seismic rebuilding. SMA bolts can achieve good SC behavior under a large strain; thus, the length of a column can be considerably reduced. The design and application of the novel SC segmental columns are highly flexible because these columns are free from excessively long PT tendons and anchorage.

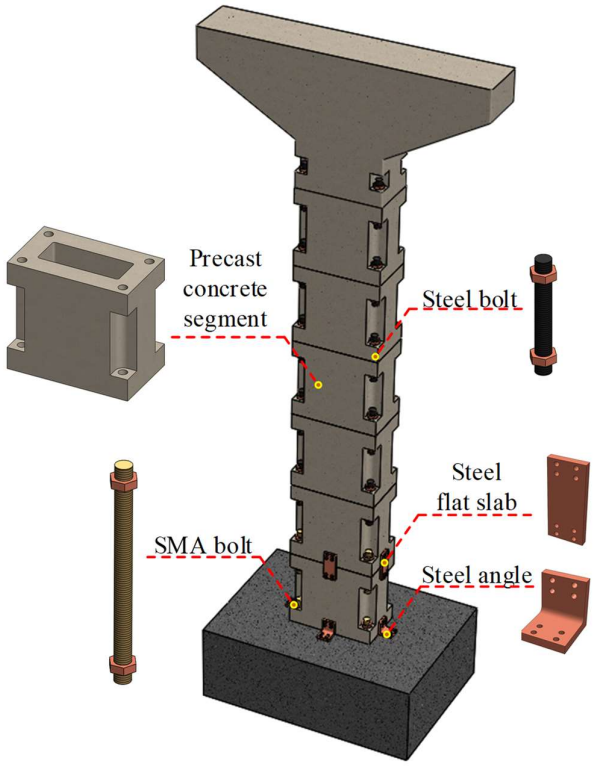

Figure 1 Configuration of SSC-PSCC

3. DESIGN AND MODELING OF SSC-PSCC

This section explains the rocking mechanism of SSC-PSCC under cyclic loading. The material properties of SMA bolts, the establishment of FEMs, and the model verification are also presented. The entire SSC-PSCC includes three core components, namely, PSCC, SMA bolts, and steel angles. Since the test results of the entire SSC-PSCC are not available at present, the modeling of these three core components was validated individually by comparing them with the previously obtained test

results.

3.1 Properties of SMA bolts

SMA is a high-performance alloy that acts as the core SC element in this novel SC segmental column due to its unique superelasticity. Phase transformation between martensite and austenite enables SMA to recover its deformation either through temperature increase (shape memory effect) or unloading (superelasticity) [36]. Superelasticity is typically preferred in civil engineering, because SMA elements can recover their residual deformation after unloading when the ambient temperature is higher than the austenite finish temperature. The hysteretic behavior of superelastic SMA is flag-shaped, effectively balancing SC and ED capacities [33].

In the current study, the FEM of the SMA bolt was built on the basis of the tests and research by Wang and Zhu [32]. A dog bone-shaped SMA bolt with a diameter of 6 mm was tested. The tested specimen followed the requirement of ASTM F2516-07. The key material parameters of the tested specimen were determined as follows: Young's modulus of austenite E_A = 36.3 GPa, Young's modulus of martensite E_M = 21 GPa, starting stress for forward transformation σ_{Ms} = 480.1 MPa, finishing stress for forward transformation σ_{Mf} = 630.2 MPa, starting stress for reverse transformation σ_{As} = 345.1 MPa, finishing stress for reverse transformation σ_{Af} = 170 MPa, Poisson's ratios for austenite and martensite (both set as 0.33), and maximum transformation strain ε_l = 2.6%. The SMA bolt exhibited typical SC flag-shaped behavior, and no fracture was found up to 7.3% strain. These key parameters obtained in the literature [32] were used in establishing a refined FEM in Abaqus in the current study. The simulation and test results are compared in Figure 2(b). The FEM exhibited good agreement with the test result and could be effectively used in subsequent research.

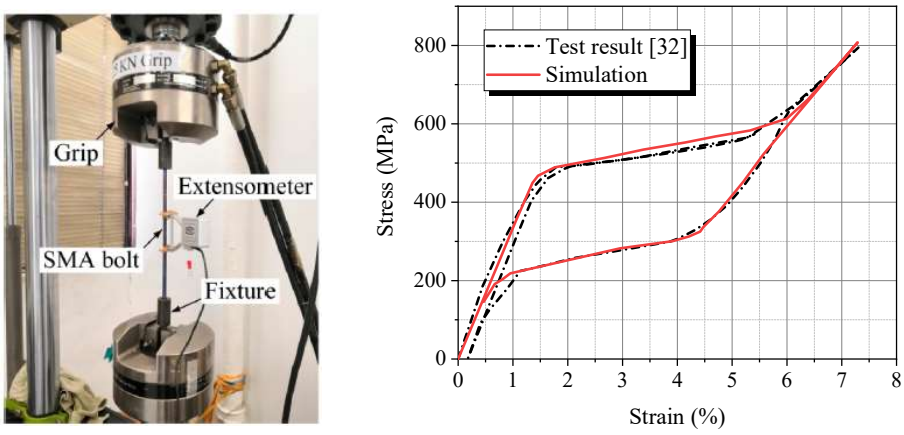

(a) (b)

Figure 2 Property of SMA bolts: (a) test setup [32] and (b) comparison between the test and simulation results

3.2 Cyclic behavior of steel angles

Steel angles are used as ED elements in the novel SSC-PSCC. Placed at the bottom of the whole column, steel angles undergo cyclic tensile–compressive deformation during earthquakes. To better simulate the behavior of steel angles, the FEM of the steel angles established in this study was first verified through the comparison with the cyclic test conducted by Wang and Zhu [32]. The specimens are two 75 mm × 75 mm × 5 mm steel angles with a yield strength of 305.3 MPa and a Young's modulus of 200 GPa. The test setup, FEM establishment, and comparison between the test and

simulation results are depicted in Figure 3. The detailed descriptions of the test can be found in a previous paper [32]. Here, only the comparison between the test and simulation results is presented. The deformation and hysteretic behavior of the simulation can fit the test results well, indicating the effectiveness of the refined FEMs. Furthermore, bolt connections were simulated as tie connections in the subsequent large-scale FEMs to balance accuracy and efficiency. Previous studies [37] have proven that such simplification would not evidently influence the global behavior of steel angles; and important behavior, such as bending and yielding in the vertical and horizontal legs, can still be reflected.

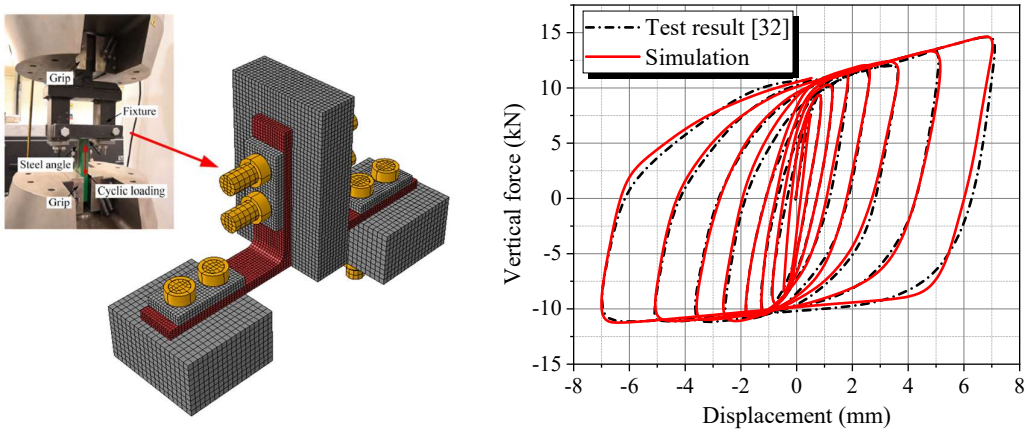

(a) (b)

Figure 3 Test and FEM of steel angles: (a) test setup [32] and FEM and (b) comparison between test and simulation results

3.3 Simulation of the segmental concrete column

The FEM of PSCC was also established and verified in the study. The cyclic test on a PSCC conducted by Jia et al. [38] was selected. The tested prototype specimen was a traditional 30-m-tall PSCC equipped with PT tendons and ED bars, and was then sclaed to a laboratory model with a scale ratio of 1:10. The column model was composed of six segments (with each segment being 500 mm tall) and a loading block (300 mm tall). The total height of the column model (without the loading block and foundation) was 3000 mm, with four PT tendons and eight ED bars crossing through the entire height. The unbonded PT tendons were anchored at the top loading block and base block. To guarantee gap opening and closing, the ED bars were unbonded with a height of 200 mm at the two bottom gaps, but they were bonded with each segment at other places through post-pouring. Apart from the PT tendons and ED bars, each segment was reinforced via basic reinforcement, and extra reinforcement was added to the base block and loading block to make them stiffer. Concrete compressive strength was 30 MPa. The steel yield strengths were 294 MPa and 364 MPa for the hoop and longitude rebar, respectively, and 392 MPa for the ED bars. Finally, the yield force of the PT tendon was 1678 MPa. The detailed description and discussion of the test can be found in the reference [38]. Only the FEM establishment and verification related to this study are presented here.

The FEM establishment, hysteretic behavior comparison, and concrete failure simulation are shown in Figure 4. The stiffness, strength, and ED capacity of the traditional PSCC can be traced well, but the SC capacity of the test is slightly weaker, largely due to the loss of prestress force. In this test, about 30% prestress force was lost, causing significant deterioration in SC capacity [38]. Such

prestress force loss was not simulated in the simulation, but its effect was limited and would not weaken the effectiveness of the whole FEM. More important, the PT tendons will not be used in the modeling of SSC-PSCC presented in the current study. The simulated deformation is shown in Figure 4(c), which illustrates the damaged locations at the bottom corners that are in accord with the test results. In the test, the gap opening of the whole structure was mostly at the bottom, and concrete crushing could be evidently observed. The verification of the FEM showed that the refined model could effectively simulate the hysteretic and damage behavior of the test, and thus it could be effectively used in the following sections.

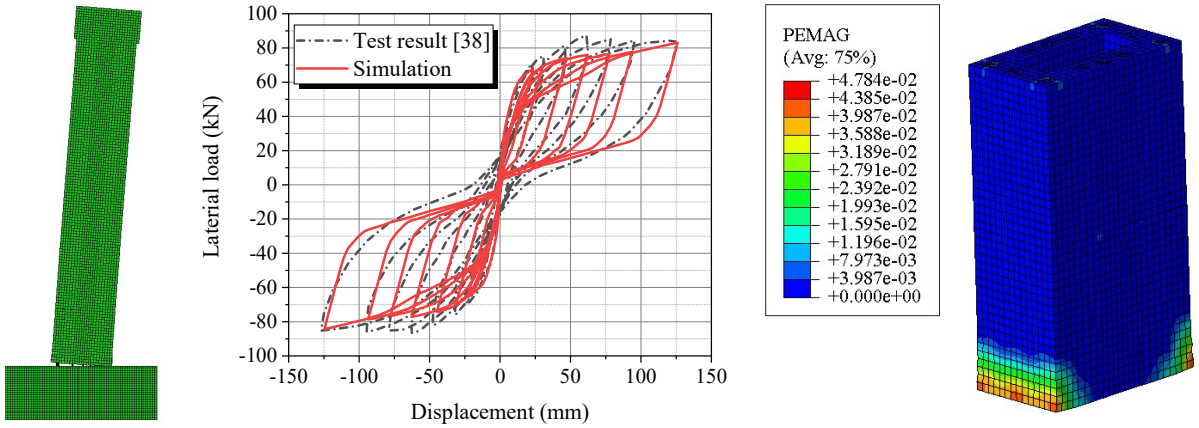

(a) (b) (c)

Figure 4 FEM and comparison with traditional precast segmental concrete column: (a) deformation of SC-PSCC, (b) hysteretic comparison between the test and simulation results, and (c) concrete damages of the bottom segments

3.4 FEM establishment of the novel SSC-PSCC

With the FEM establishment approaches for individual components verified through the previous tests, the FEM of the novel SSC-PSCC can be finally assembled. The basic design of the SSC-PSCC, including the segment width, height, length, and number of segments, follows that of Jia's test [38] mentioned in Section 3.3. The detailed designs are shown in Figure 5. The whole segmental column is connected by SMA bolts and steel bolts with a diameter of 20 mm. To balance seismic performance and monetary cost, SMA bolts are only installed at two bottom gaps, while other segments are connected by steel bolts. All the bolts are 200 mm long, while the base bolts connecting the bottom segment and foundation are 450 mm long to allow a large gap opening at the base. Four steel angles with dimensions of 200 mm × 200 mm × 60 mm × 15 mm (vertical leg × horizontal leg × width × thickness) are selected to enhance ED capacity, and four corresponding steel flat plates with dimensions of 200 mm × 60 mm × 15 mm (height × width × thickness) are added to enhance the gap-opening force at the second gap (counted from the base) and make the major gap opening occur at the base. The reinforcement in the segments is shown in Figure 5, wherein four large ducts can be found at the corners. The diameter of a duct is slightly larger than that of a bolt for easy installation, and four rebars with a diameter of 12 mm are placed around the duct to guarantee that the bolts and segments work together. Notably, all the rebars are cut off at the gap, and the bolts are the only connection. The displacement-controlled cyclic loading is applied at the middle point of the loading block, and the height between the loading point and the base is 3150 mm. The loading protocol in the

simulation follows the testing protocol shown in Section 3.3, and the maximum target displacement is 126 mm (corresponding to a 4% drift ratio). Moreover, an axial force is added to simulate the vertical loading transferred from upper structures. In most bridge columns, the axial load index (ALI, defined as the ratio between the axial load to the compressive strength of the column) ranges from 0.05 to 0.15 and should not exceed a value of 0.3 [39, 40]. Therefore, an ALI of 0.13 is selected on the basis of the test. The concrete damaged plasticity (CDP) material model is used for concrete simulation; the CDP model has been proven to be accurate and effective in concrete damage simulation [15]. The ideal elastoplastic material model is used for the steel rebars and elements [41], and the superelastic material model is used for the SMA bolts [30]. The key parameters of the material model are provided in Table 1, and the steel strength used in the steel ED elements is lower than those of the steel bolts and rebars to maintain early yielding and better ED capacity. All the major elements, including the concrete segments, SMA bolts, steel bolts, and steel angles, are simulated using C3D8R solid elements [42], and the steel rebars are simulated by 3D truss elements [43]. Finally, a low initial prestrain (about 0.02%) is added to all the SMA and steel bolts to simulate the tightening force in practice.

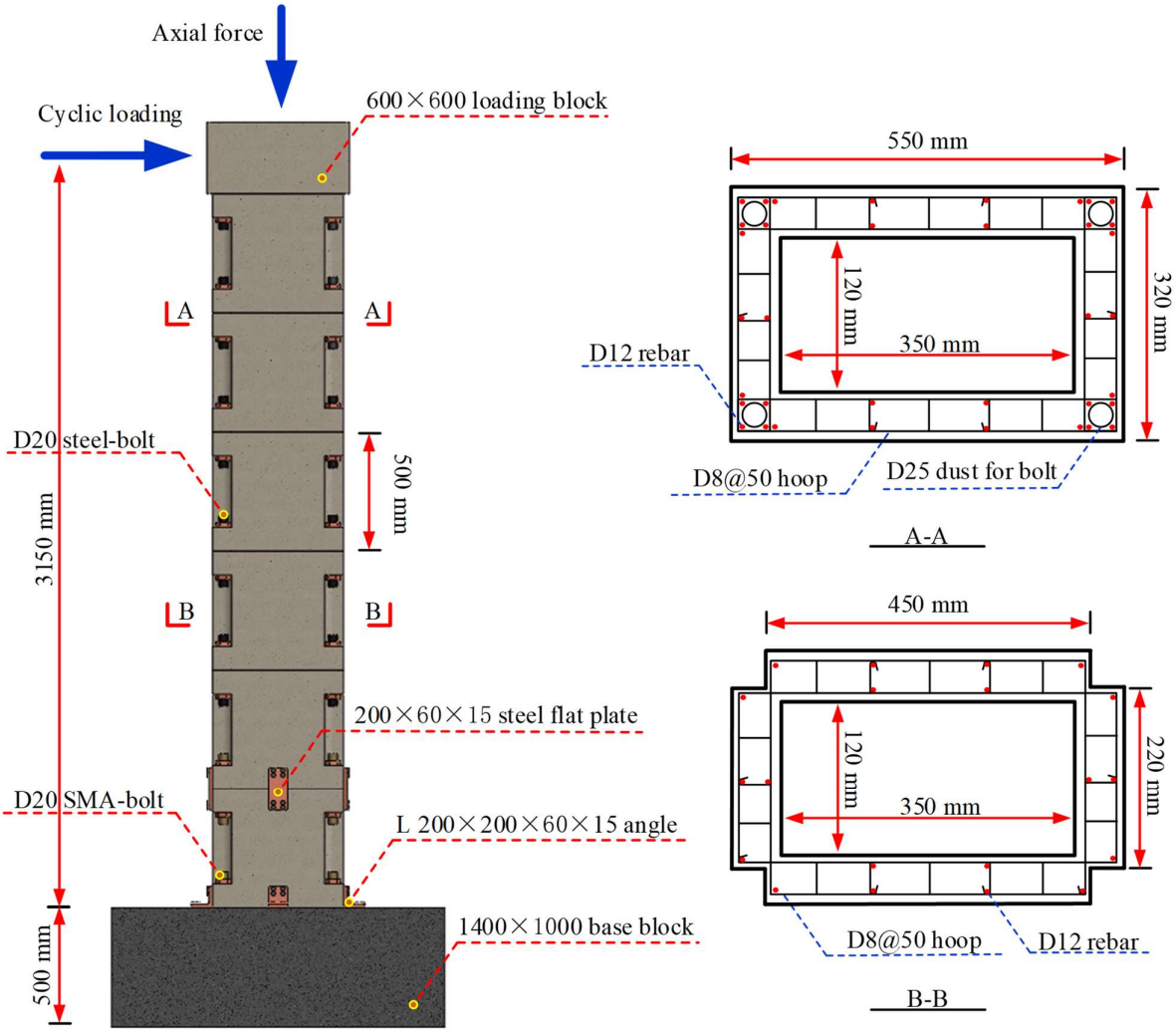

Figure 5 Design of the benchmark SSC-PSCC

Table 1 Key material parameters used in the simulation

Parameters	Symbol	Selected value
Concrete		
Young's modulus	E_c	36 GPa
Poisson's ratio	v_c	0.2
Strength	f_c	38.5 MPa
Steel rebars		
Young's modulus	E_s	200 GPa
Poisson's ratio	v_s	0.3
Yield strength	f_s	435 MPa
Post-yield stiffness ratio	α	0.01
Steel angles and slab plates		
Young's modulus	E_{sa}	210 GPa
Poisson's ratio	v_{sa}	0.3
Yield strength	f_{sa}	270 MPa
Post-yield stiffness ratio	α_a	0.01
Steel bolts		
Young's modulus	E_{sa}	200 GPa
Poisson's ratio	v_{sa}	0.3
Yield strength	f_{sa}	900 MPa
Post-yield stiffness ratio	α_a	0.01
SMA bolts		
Young's modulus of austenite	E_A	26.0 GPa
Young's modulus of martensite	E_M	16.0 GPa
Starting stress for forward transformation	σ_{Ms}	340.1 MPa
Finishing stress for forward transformation	σ_{Mf}	415.5 MPa
Starting stress for reverse transformation	σ_{As}	220.2 MPa
Finishing stress for reverse transformation	σ_{Af}	60.0 MPa
Poisson's ratio	v_A / v_M	0.33
Maximum transformation strain	ε_l	2.5%

4. SIMULATION RESULTS

4.1 Simulation results of SSC-PSCC

The hysteretic behavior of SSC-PSCC is illustrated in Figure 6. The hysteretic curve exhibits a typical flag-shaped behavior, indicating the effectiveness of the SMA bolts placed at the bottom gaps of the whole segmental columns. Compared with the typical fat hysteretic curves of traditional cast-in-place columns, the flag-shaped hysteretic curve provides a moderate ED capacity with limited residual deformation. As shown in Figure 6, the maximum residual deformation is 13 mm (0.4%), which is considerably smaller than the repairable threshold value of 1% [44], indicating the excellent SC capacity of SMA bolts. The recovery ratio (defined as the ratio between the recovered

deformation and the peak deformation) of SSC-PSCC is generally higher than 90%, i.e., 90% of the total deformation can be recovered after unloading. ED capacity can be measured via the equivalent viscous damping ratio, which is defined as the ratio between the total energy dissipated per cycle and the elastic strain energy absorbed in an equivalent linear system at the same peak displacement and force. The equivalent damping ratio is up to 17.9% at the maximum target displacement, considerably beyond the threshold value of 8% required in ACI 550.6 [45]. An evident two-stage yielding can be observed in the hysteretic curve, representing the yield of the steel angles and SMA bolts, respectively. In the beginning, the SMA bolts and steel angles are elastic, and a large initial elastic stiffness can be observed. After reaching the yield point of the steel angles, an evident stiffness decrease can be recorded, and the ED capacity of SSC-PSCC is activated. While displacement further increases to about 50 mm, as shown in Figure 6(b), the transformation strain of the bottom SMA bolts is reached, and a flat platform can be seen in the hysteretic curves. This type of two-stage yielding pattern presents a balance between the ED and SC capacities of SSC-PSCC by properly considering the material characteristics of SMA and steel. In most SMA-based SC structures, the SMA elements act as the crucial SC elements and provide moderate ED capacity, while the additional ED elements dissipate the major input energies. Furthermore, the phase transformation strain of typical SMA is around 1%, and the valid SC range of SMA is generally restrained under 6% to 8% strain, which is smaller than the maximum tensile strain of steel (over 10%) [46]. Therefore, the early yielding of the ED steel angles can promote the ED capacity of SSC-PSCC in the early stage, and it exhibits no failure risk in the working stage.

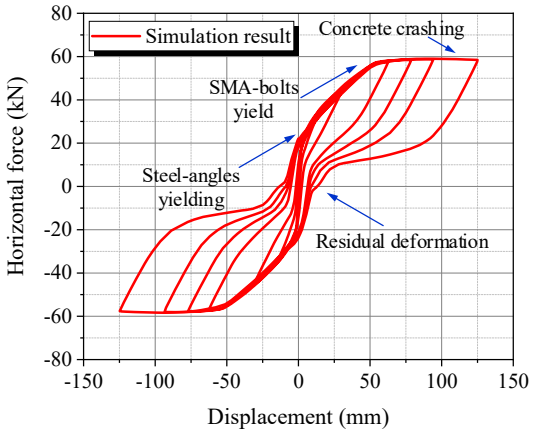

(a)

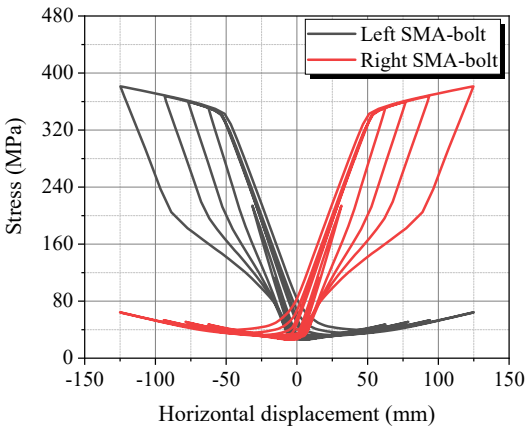

(b)

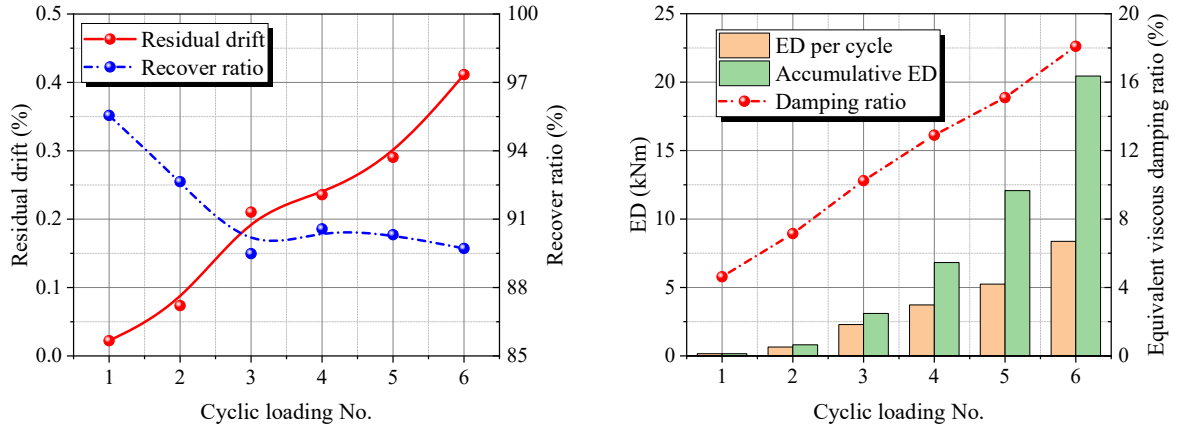

(c) (d)

Figure 6 Hysteretic behavior of the novel SSC-PSCC: (a) horizontal force–displacement relationship of the entire structure, (b) bolt stress–column displacement relationship of SMA bolts, (c) residual drift per cyclic loading of the entire structure, and (d) ED of the entire structure (ED per cycle and accumulative ED)

The deformation of SSC-PSCC at the maximum target displacement is shown in Figure 7. Most of the structural deformation is contributed by the bottom gap opening, effectively activating the ED steel angles and achieving the design targets. With the help of steel flat slabs, the gap opening at the second segment is restrained, guaranteeing that nearly all the plastic deformations occur only in the bottom steel angles and protecting other parts of SSC-PSCC from damage. Under a horizontal force, the column's deformation and ED are mostly induced by the extension of the bottom SMA bolts, the bending of steel angles, and the rigid body rotation of segments, ensuring that other steel bolts are mostly connection elements and remain elastic during the whole loading phase. After unloading, the SMA bolts can recover to their initial shape, and a quick replacement of the steel angles can fully recover the structural function of SSC-PSCC, largely increasing structural resilience and reducing monetary loss during earthquakes and post-seismic rebuilding.

The stress distributions of the steel angles are presented in Figure 7. Figure 7(b) shows the stress distributions of the steel angles at the maximum target displacement. The maximum stress of the angles is concentrated in the area near the fillet part and the connection part with the segments; this finding is highly consistent with previous tests and simulations [30, 47]. The maximum stress of the steel angles is 400 MPa, exceeding the yield stress of 270 MPa but still free from any fractures during the loading (the maximum plastic strain of the steel angles is 3%, causing some unrecoverable deformations in structures but largely smaller than the maximum tensile strain of the steel). Therefore, the steel angles can fully satisfy ED and reliability demands during loading, and a rapid replacement can fully recover the structural function.

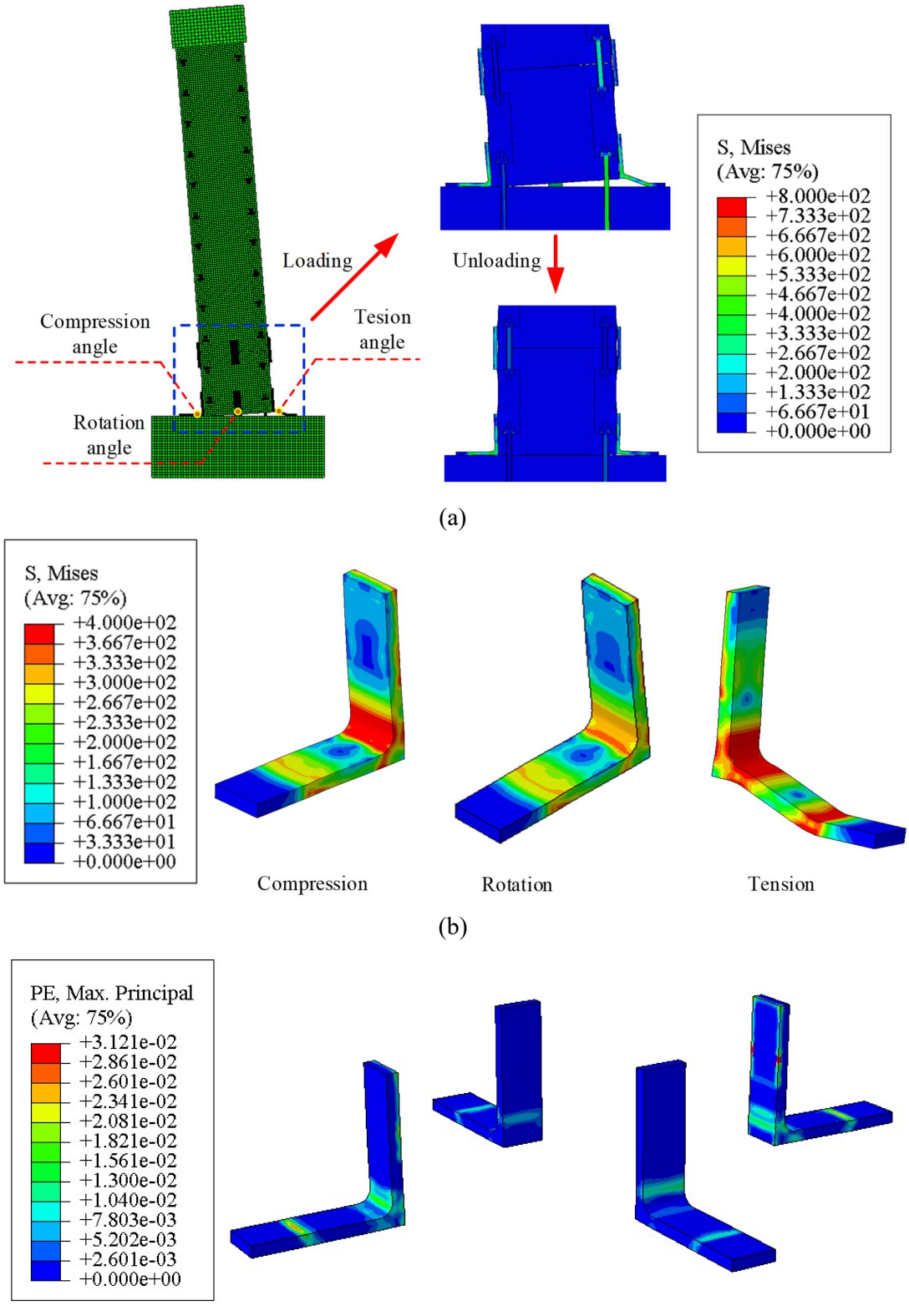

Figure 7 Deformation and stress condition of SSC-PSCC: (a) overall condition of the structure, (b) detailed stress condition of the angles while loading, and (c) detailed plastic strain condition of the

angles while unloading

The stress distribution of the bottom SMA bolts is shown in Figure 8. In the maximum target displacement, the tensile stress of the SMA bolts in tension is 393 MPa, which is higher than the starting stress of phase transformation but lower than the finishing stress of phase transformation. Therefore, the SMA bolts can provide a moderate ED capacity due to phase transformation and can fully recover their original shape upon unloading. For the relaxed SMA bolts, a low tensile stress can be found [around 30 MPa, as shown in Figure 6(b)], which is caused by the initial tightening stress of the bolts. Figure 8(b) illustrates the stress distribution of the SMA bolts after unloading completely. A small amount of stress (around 80 MPa) can be observed, which is the recovery force provided by the SMA bolts to help the steel angles back to their original states. From the stress condition analysis, the stress level of the SMA bolts is within the platform of phase transformation, providing a secondary ED capacity and excellent SC capacity, verifying that the design of SSC-PSCC is appropriate.

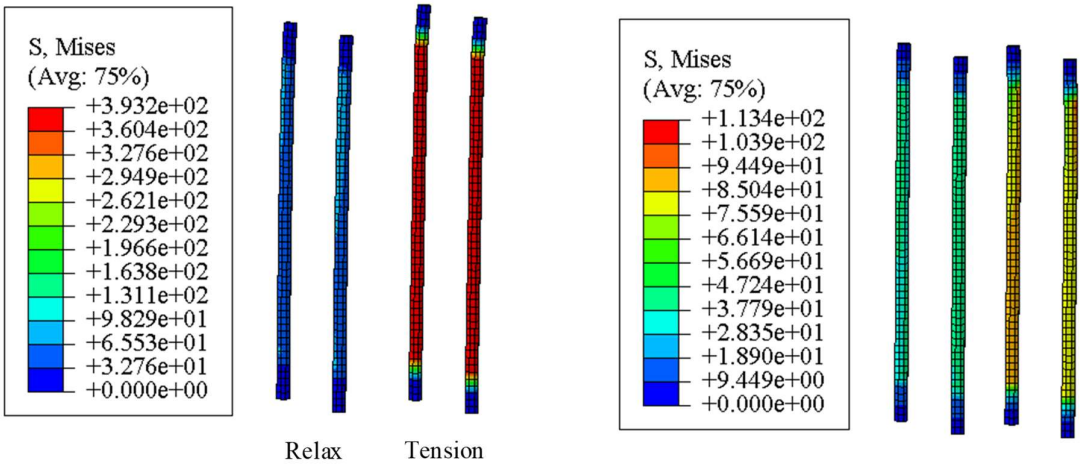

(a) (b)

Figure 8 Bottom SMA bolt stress condition: (a) at maximum target displacement and (b) at initial location

Figure 9 shows the stress distribution of the steel flat slabs and SMA bolts at the second gap. Except for the stress concentration in a few parts, nearly all the steel and SMA elements are in elastic phase, demonstrating that adding extra steel flat slabs is effective in restraining the opening at this gap. After adding steel flat slabs to the second gap, the gap-opening force of this gap is considerably larger than that of the base gap, ensuring inelastic deformation concentration at the base. Due to limited bolt length and no ED elements at the second gap, a large opening at the second gap may evidently compromise the structural performance of SSC-PSCC. This phenomenon is further discussed in the following parametric analysis.

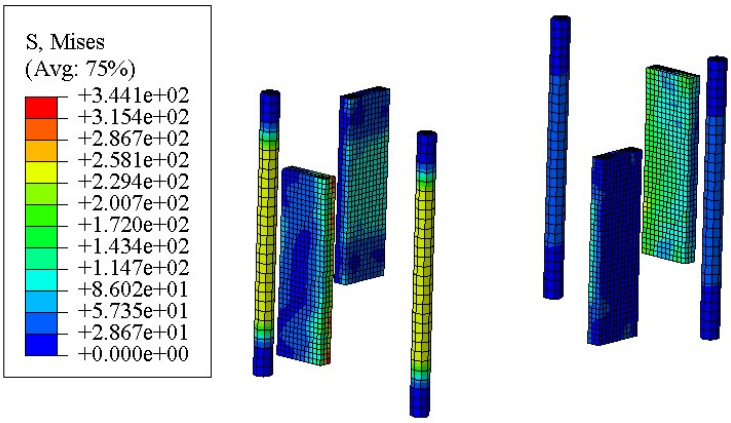

Figure 9 Stress condition of the steel flat slabs and SMA bolts at the second gap under maximum target displacement

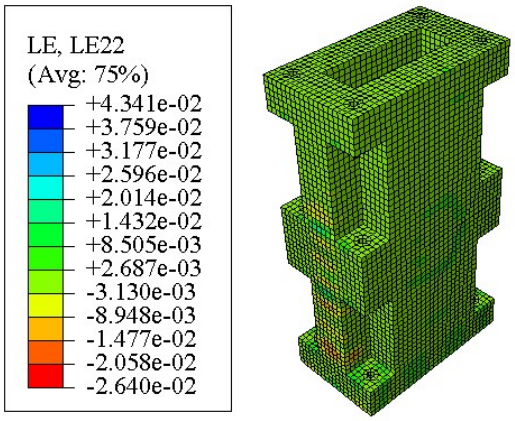

Figure 10 Strain condition of the concrete segments under maximum target displacement

The strain distribution of the two bottom concrete segments are shown in Figure 10. The maximum compressive strain is around 1.5%, showing that the crushing of the surface concrete may occur locally. This phenomenon was also observed in the previous test of a PT-based PSCC [38], which caused a strength decline in the hysteretic curves (Figure 6), prestress loss in PT tendons, and the partial loss of SC capacity. However, the SC capacity of SSC-PSCC relies on SMA's superelastic property instead of PT. Thus, the influence of concrete crushing is relatively inevident compared with PT-based PSCC. Therefore, the safety and reliability of SSC-PSCC can be guaranteed.

4.2 Comparison between SSC-PSCC and traditional PT-based SC-PSCC

The comparisons between SSC-PSCC and the traditional PT-based SC-PSCC are provided in Figure 11. The SC and ED capacities of these two types of segmental columns are similar. The residual drift ratio of the traditional PT-based segmental column is slightly larger due to its PT loss, and the ED capacity of SSC-PSCC is smaller at first due to the later activation of SMA phase transformation. When achieving similar structural performance, the novel SSC-PSCC exhibits some unique advantages. First, in the traditional PT-based SC-PSCC, replacing the embedded damaged ED bars or fixing the PT cables is difficult. In contrast, the bolt-connected design of SCC-PSCC that

is free of any PT anchorages requires a considerably simple process in on-site construction and thus will facilitate practical applications greatly. Moreover, all the ED and SC elements of SSC-PSCC can be repaired or replaced easily if necessary, making the recovery of the structural function more convenient. Second, the SC behavior of SSC-PSCC is primarily attributed to SMA material property instead of the PT technique. Therefore, the good fatigue behavior of SMA helps SSC-PSCC to be free from the potential SC loss induced by PT losses. After an earthquake, the SMA bolts can recover to their original shape, while the steel angles can be simply replaced. The structural function can be nearly recovered to its original state. Third, the ED bars exhibit a large residual deformation, while the PT cables produce a large recovery force. This recovery force applies a large compression on the ED bars and may cause buckling in the unbonded region, as shown in Figure 11(c). Under a large seismic intensity, the surface concrete may be crushed, further weakening the restraint on the ED bars. Consequently, the ED bar buckling may cause the breaking on the segment surface. In SSC-PSCC, however, the flag-shaped behavior of the SMA bolts guarantees that the bolt stress is extremely small when they are back to their original state, as shown in Figure 11(d), and the bending behavior of steel angles is also free from buckling. Lastly, the use and design of SSC-PSCC are more flexible.In the PT-based SC-PSCC, the PT cables should be sufficiently long to accommodate deformation and maintain elasticity. But a 4% drift may cause the yielding of the PT cables in some short columns, even if the PT cables runs from the column top to bottom. In SSC-PSCC, however, the SMA bolts are considerably shorter (450 mm in the simulated case), making the design and construction much easier. Therefore, the novel SSC-PSCC is a promising SC structural system for future applications. The succeeding sections focus on the influences of several crucial design parameters.

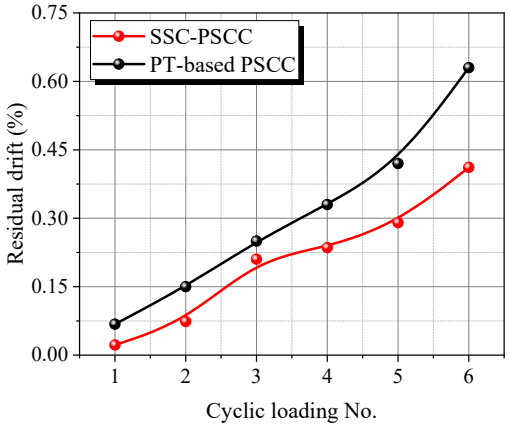

(a)

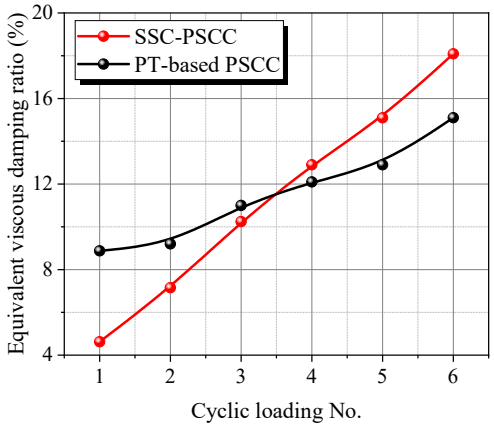

(b)

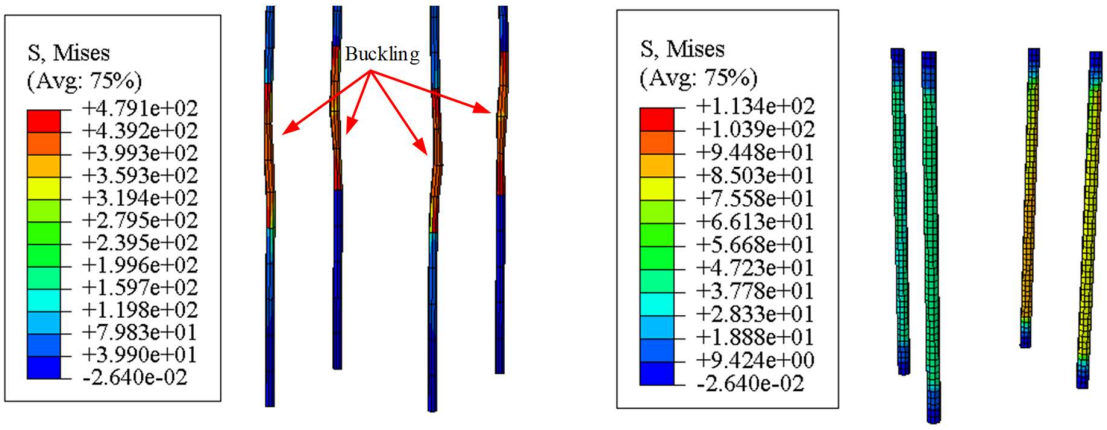

(c) (d)

Figure 11 Comparison between SC-based and PT-based segmental columns: (a) SC capacity, (b) ED capacity, (c) stress and deformation of ED bars in traditional PT-based SC segmental column when completely unloaded, and (d) stress and deformation of SMA bolts in the novel SSC-PSCC when completely unloaded

5. PARAMETRIC STUDY OF SSC-PSCC

Parametric studies were conducted to further investigate the performance of SSC-PSCC. Twelve FEMs (including the baseline model presented in Section 3.4) with different design parameters were analyzed, and their performance under cyclic loads was compared with that of the baseline model. The design parameters of eight FEMs are provided in Table 2. The considered design parameters included the prestress levels in the SMA bolts (SC-2 and SC-3), ALI of the column (SC-4 and SC-5), and the diameters of longitudinal rebars in the segments (SC-6, SC-7, and SC-8). Another important parameter, the stiffness ratio between steel elements and SMA elements, is properly tuned to balance ED capacity and residual deformation [48]. The detailed results and discussions are presented below.

Table 2 Design parameters of different FEMs

Specimens	Prestrain in bolts	Segments connected by SMA bolts	ALI	Steel flat slab thickness	Longitudinal rebar diameter in segments
SC-1*	0.02%	Bottom two segments	0.13	15 mm	D12
SC-2	0.00%	Bottom two segments	0.13	15 mm	D12
SC-3	0.04%	Bottom two segments	0.13	15 mm	D12
SC-4	0.02%	Bottom two segments	0.26	15 mm	D12
SC-5	0.02%	Bottom two segments	0.065	15 mm	D12
SC-6	0.02%	Bottom two segments	0.13	15 mm	D8

SC-7	0.02%	Bottom two segments	0.13	15 mm	D6
SC-8	0.02%	Bottom two segments	0.13	15 mm	D16

* The baseline model simulated in Section 3.

5.1 Prestrain in bolts

The hysteretic behavior of S-1, S-2, and S-3 specimens is shown in Figure 12, reflecting the influence of bolt prestrain. When increasing bolt prestrain from 0.02% to 0.04%, initial structural stiffness slightly increases from 11.98 kN/mm to 12.24 kN/mm. Structural strength increases by about 0.5%, i.e., from 59 kN to 59.27 kN, and residual drift decreases from 13 mm to 12.9 mm. When removing all bolt prestrain, structural stiffness decreases to 11.7 kN/mm, and structural strength and residual deformation are nearly the same. In general, the prestrain level in the bolts influences initial structural stiffness slightly, but exerts minimal influence on structural strength and residual drift. As shown in Figure 12(b), increasing the bolt prestrain only leads to higher initial stress at zero displacements and causes early phase transformation. However, it does not impact other important parameters, such as the ED and SC capacities. In contrast with traditional PT-based SC structures, the SC capacity of SMA is due to its unique superelastic behavior, and a large level of prestrain is not required. Furthermore, the working range of the SC capacity of SMA (up to 6% to 8%) is considerably larger than the yield strain of steel (around 0.2%). Therefore, a small bolt prestrain can only influence the initial performance of SMA bolts, but exerts minimal effect on the overall ED and SC capacities. Notably, a certain level of bolt prestrain is still necessary to maintain friction between the segments to resist shear force. In the current study, however, structural performance is dominated by bending and rigid rotation, and the influence of shear behavior is inevident. The shear resistance behavior is important in some other cases (e.g., unexpected crushing in bottom segments) [49]. But it is outside the major scope of this work and will be investigated in future studies.

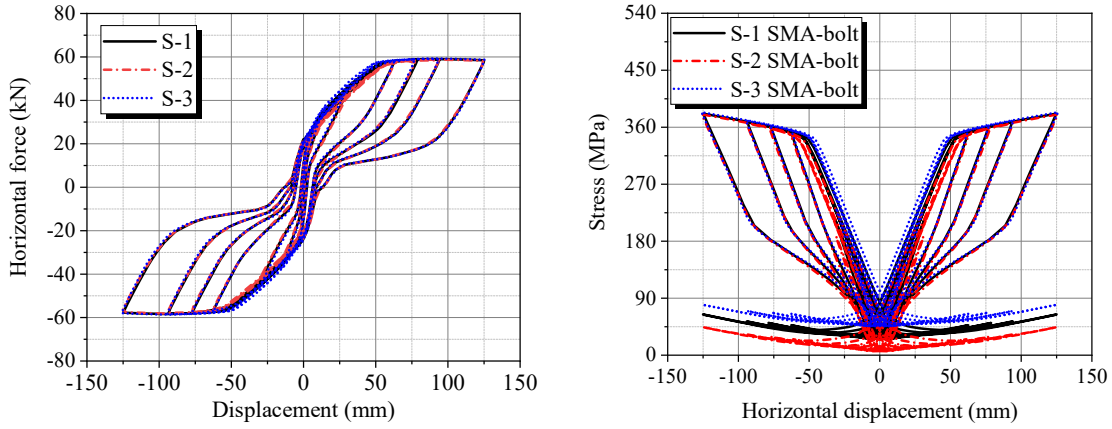

(a) (b)

Figure 12 Hysteretic curves of S-1, S-2, and S-3 specimens: (a) performance of the entire structure and (b) performance of the SMA bolts

5.2 ALI

The influence of ALI is discussed in this subsection. ALI is an important factor in all vertical structures. The ALI of bridge piers typically ranges from 0.05 to 0.15 and cannot exceeds 0.3 [39, 40].

Three different ALI values, i.e., 0.13 (S-1), 0.26 (S-4), and 0.065 (S-5), were selected to represent moderate, large, and small ALI, respectively. As shown in Figure 13, the influence of ALI is evident and omnifarious. With an increase in ALI, structural stiffness and strength increase, generally caused by an increment in the gap-opening force. In large ALI, an equivalent extra PT strength is added to the structure, and a larger horizontal force is necessary to reach the target displacement. Furthermore, a larger ALI causes lower residual deformation (i.e., a higher SC capacity), as shown in Figure 13(c). The residual deformations at the last cycle for S-1, S-4, and S-5 are 12.96, 12.01, and 17.01 mm, respectively, and they generally decrease with the increasing ALI. As shown in Figure 13(b), the behavior of SMA bolts is similar in all three specimens. A small ALI leads to the relaxation of the prestrain on the compressive side. However, such prestrain relaxation becomes minimal under moderate and large ALI. Meanwhile, other important parameters, such as the phase transformation strain, ultimate strength, ED capacity, and SC capacity of SMA bolts, are nearly the same. From the preceding discussions, a larger ALI may increase the stiffness, strength, and SC capacity of SSC-PSCC, but some shortages can also be found. In Figure 13(a), an apparent negative tangential stiffness can be found in the S-4 specimen at a large displacement; while in S-5, the stiffness after SMA bolt yielding remains positive. The P-Δ effect caused by the vertical force is the primary reason. The vertical axial force behaves as a recentering force at a small displacement, but it becomes harmful to the recentering at a large displacement and generates a negative stiffnes. Furthermore, a large ALI causes more severe damage in concrete segments. As shown in Figure 14, considerably larger damage can be found in S-4 Compared with the concrete damage of the baseline specimen shown in Figure 10, an increase in ALI causes an increase in concrete damage. In 0.26 ALI, the compression strain of the concrete reaches 0.0264, showing that this part of the concrete is completely crushed. Concrete crushing may increase the ED capacity of the entire structure, as shown in Figure 13(d). However, it will bring many complicated problems in post-seismic repair. In the SSC-PSCC design, all the damages are proposed to concentrate in the steel angles, and a large range of concrete crushing in segments is undesirable for complex replacement and repair. Therefore, ALI beyond the general range of 0.15 is not recommended in the design. In S-5 with a small ALI, ED and SC capacities decrease slightly, but still within an acceptable range. Therefore, SSC-PSCC can achieve the design target within the commonly used ALI range.

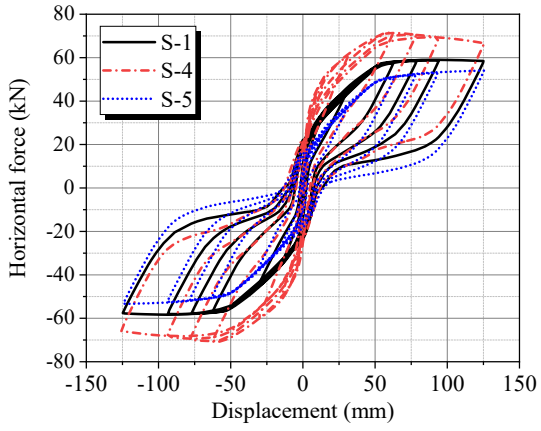

(a)

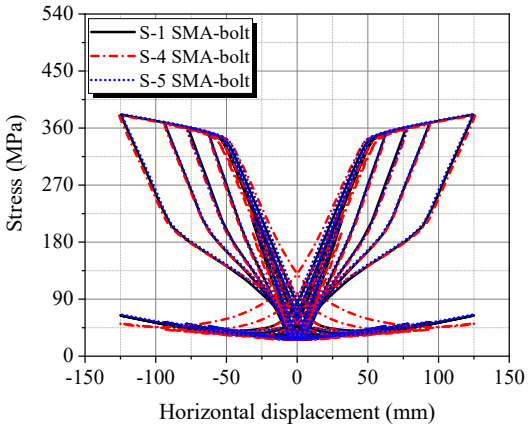

(b)

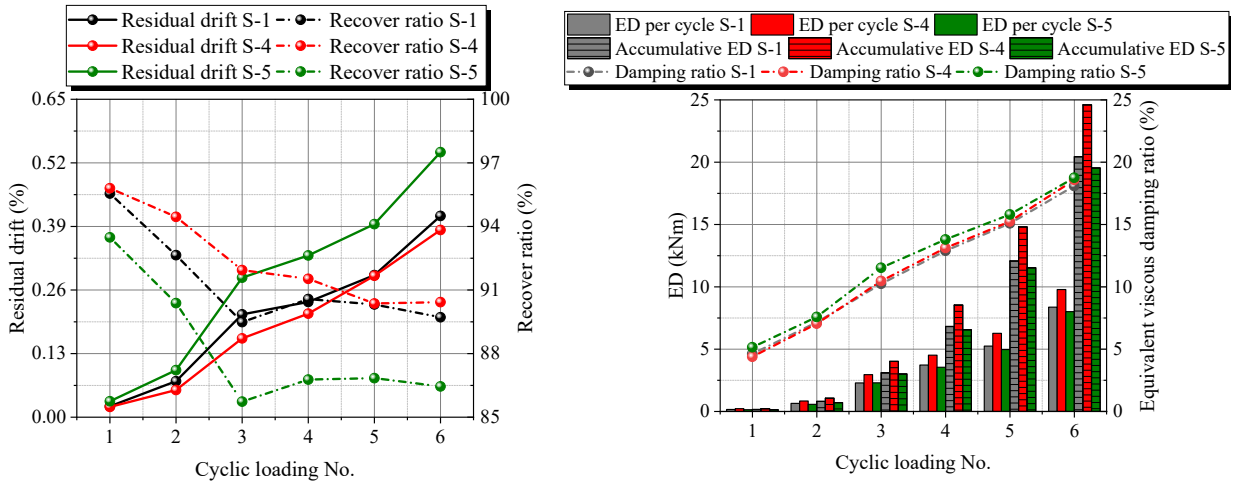

(c) (d)

Figure 13 Hysteretic behavior of specimens with different ALI values: (a) entire structures, (b) SMA bolts, (c) SC capacity, and (d) ED capacity

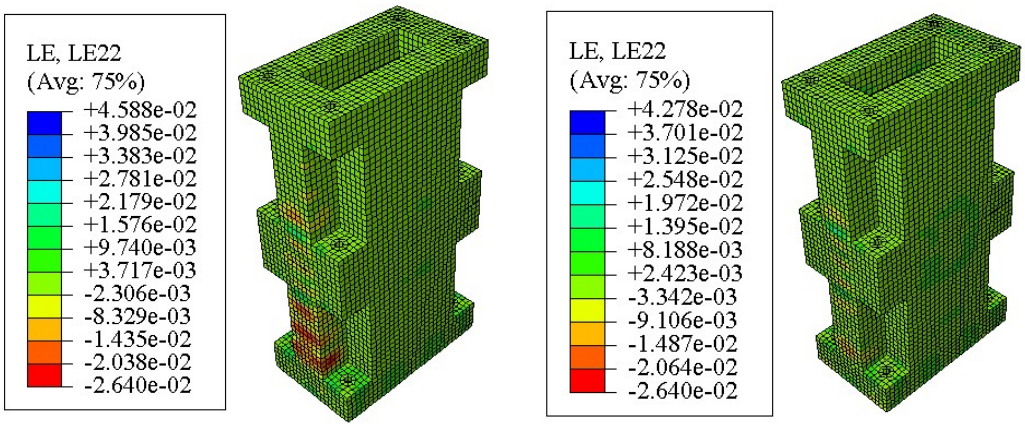

(a) (b)

Figure 14 Concrete damage situation at maximum target displacement: (a) S-4 specimen and (b) S-5 specimen

5.3 Diameter of longitudinal rebars in the segments

The last parameter is an important but easily overlooked one, i.e., the diameter of the longitudinal rebars in the segments. In the design assumption of SSC-PSCC, the segments are regarded as rigid and only undergo rigid body rotation. However, this assumption can only be achieved when the designed segmental stiffness is considerably larger than SMA bolts. Thus, the segmental stiffness should be guaranteed by reinforcement.

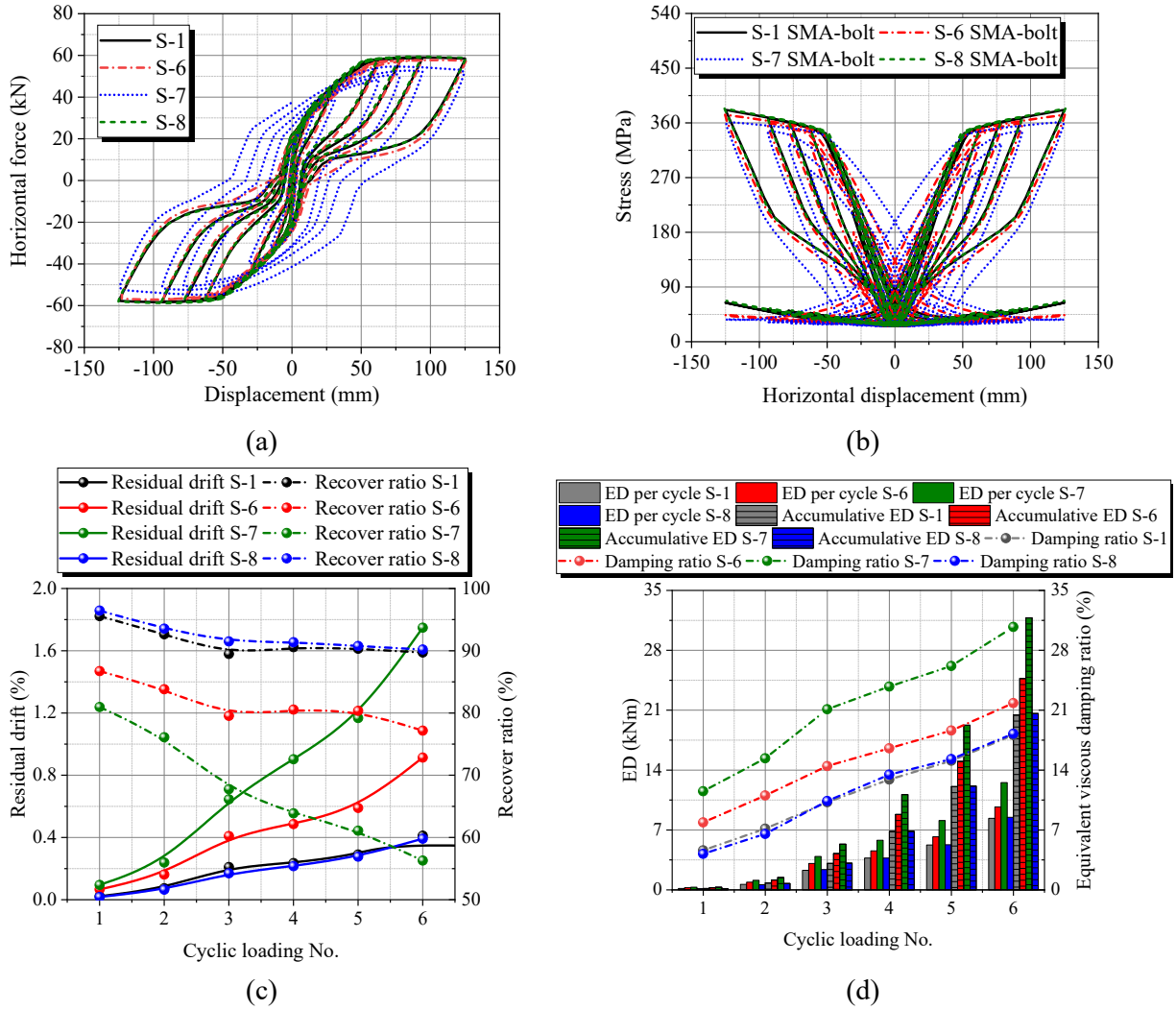

Figure 15 Performance of the S-1, S-6, S-7, and S-8 specimens: (a) hysteretic performance of the entire structure, (b) hysteretic performance of SMA bolt, (c) SC capacity, and (d) ED capacity

Figure 15 and Figure 16 show the structural performance of the S-1, S-6, S-7, and S-8 specimens. The design bending strength of the segments of the four specimens are 132, 59, 33, and 234 kNm, respectively, and the bending strength provided by the SMA bolts is 120 kNm at the end of phase transformation. In Figure 15(a), a decrease in rebar diameter causes an evident degradation in structural strength and SC capacity. As shown in Figure 16, the steel reinforcement is elastic when reaching the maximum target displacement (yield stress is 435 MPa). When the rebar diameter (S-6) decreases, the stress of the steel rebars increases considerably, exceeding the yield point. Therefore, plasticity development can be observed in the segments, and the rigid body assumption and integrity of SSC-PSCC are compromised. Moreover, the SC capacity, stiffness, and strength of SSC-PSCC and the stress in SMA bolts decrease. When the diameter of the reinforcement further decreases (S-7), the stress of the rebars largely exceeds the yield point, and structural hysteretic curves are more likely a traditional cast-in-place column without an added SC element (a large ED capacity but SC capacity

is sacrificed). The deformation of the column is mainly contributed by the tension and compression of the steel rebars, and the SC behavior of the SMA bolts cannot be effectively activated. As shown in Figure 17, the gap opening at the base is considerably smaller than that in the baseline specimen (i.e., S-1). The significant damage in the base segment will make pose-seismic repair impossible, as the residual deformation largely exceeds the threshold value of 1%.

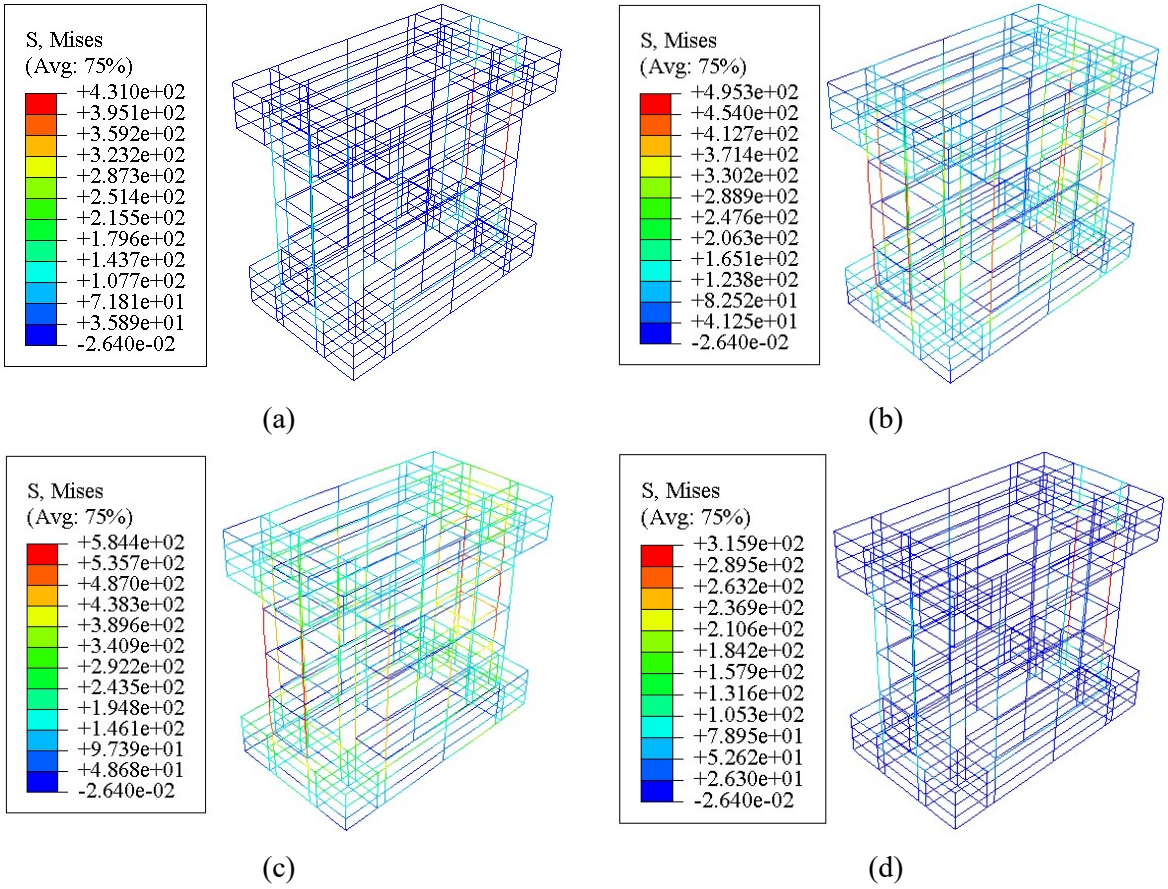

Figure 16 Stress of the steel reinforcement of the bottom segment: (a) S-1 specimen, (b) S-10 specimen, (c) S-11 specimen, and (d) S-12 specimen

Large-diameter rebars are used in the S-8 specimen. Rebar stress is considerably lower than the yield point of 435 MPa at the maximum displacement. However, the large-diameter rebars produce only a slight difference in structural performance. The rebars help to maintain a large stiffness of the segments, and a too large diameter of the rebars cannot further improve the SC and ED capacities of SSC-PSCC. Therefore, the diameter of the rebars should be properly selected so that the steel rebars can remain elastic at a large displacement when the SMA bolts finish phase transformation and enter the strain hardening stage.

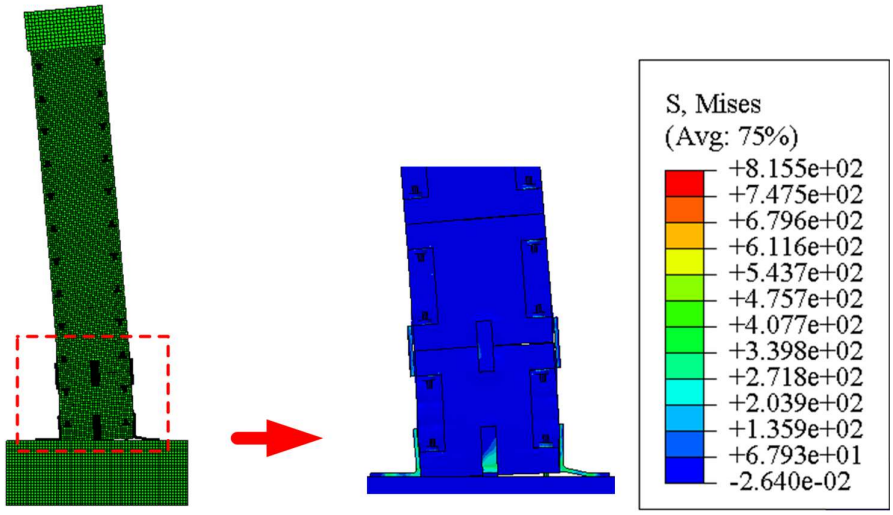

Figure 17 Deformation of the S-7 specimen at the maximum target displacement

6. CONCLUSION

A novel SSC-PSCC is proposed and investigated in this study. SSC-PSCC is connected only by using SMA and steel bolts and is completely free from post-pouring and PT elements. Additional steel angles are added to improve the ED capacity of the structure. The behavior of this novel SSC-PSCC is investigated using refined FEMs verified through previous tests. The FEMs exhibit high agreement with previous test results and are effective for subsequent studies. The hysteretic behavior of SSC-PSCC is comprehensively discussed, and 12 FEMs are used to study the influence of several crucial design parameters. Several major conclusions can be drawn as follows.

(1) SSC-PSCC exhibits a desirable and stable SC behavior. A typical flag-shaped hysteretic behavior can be observed with minimal residual deformation. The SMA bolts act as SC elements and provide moderate ED capacity, while the extra steel angles act as major ED elements. Several steel flat slabs are added to increase the gap-opening force at the second gap and thus concentrate the major gap opening at the base.

(2) The hysteretic curve of SSC-PSCC presents a three-stage stiffness due to the respective yielding of SMA bolts and steel angles. This two-stage yielding is beneficial for fully utilizing the ED capacity of steel angles and the SC capacity of SMA bolts. Furthermore, a small negative tangential stiffness at a large displacement can be observed in the hysteretic curves in large ALI case due to the P-Δ effect, but in commonly used ALI range, the influence is acceptable.

(3) Compared with the traditional PT-based PSCC, the novel SSC-PSCC can achieve similar structural performance (stiffness, strength, and ED and SC capacities) while exhibiting many advantages, such as easy construction and repair after earthquakes, quick replacement of damaged ED elements, completely free from buckling of ED bars observed in traditional PT-based segmental columns, and more flexible design and construction.

(4) Through parametric studies, the influences of several crucial design parameters are discussed. In general, the influences of prestrain level in the SMA and steel bolts are inevident. ALI exerts an obvious influence on structural performance, and a value lower than 0.15 will be favorable for structural performance. An adequate rebar diameter is crucial

for maintaining desirable SC behavior and failure mode of a structure, but over-design is unnecessary.

ACKNOWLEDGMENTS

The authors are grateful for the financial support from the Research Grants Council of Hong Kong (Grant Nos. PolyU 152246/18E and T22-502/18-R), the National Key Research and Development Program of China (Grant No. 2019YFB1600700), the National Observation and Research Station of Material Corrosion and Structural Safety of Hong Kong-Zhuhai-Macao Bridge in Guangdong, and the Hong Kong Polytechnic University (Grant Nos. ZE2L, ZVX6, and P0035787). The findings and opinions expressed in this paper are solely those of the authors and do not represent the view of the sponsors.

REFERENCES

[1] Zhong-Kui Cai, Zhenyu Wang and T.Y. Yang, *Experimental testing and modeling of precast segmental bridge columns with hybrid normal- and high-strength steel rebars.* Constructional Building Material, 2018. **166**: p. 945-955.

[2] Jia Jf, Zhang Kd and Salidi Ms, *Seismic evaluation of precast bridge columns with built-in elastomeric pads.* Soil Dynamics and Earthquake Engineering, 2020. **128**: p. 105868.

[3] Jui-Chen Wang, Yu-Chen Ou, Kuo-Chun Chang and George F. Lee, *Large-scale seismic tests of tall concrete bridge columns with precast segmental construction.* Earthquake Engineering and Structural Dynamics, 2008. **37**: p. 1449-1465.

[4] Chao Li, Hong Hao and Kaiming Bi, *Seismic performance of precast concrete-filled circular tube segmental column under biaxial lateral cyclic loadings.* Bulletin of Earthquake Engineering, 2019. **17**: p. 271-296.

[5] Jun Li, Hong Hao and Chengqing Wu, *Numerical study of precast segmental column under blast loads.* Engineering Structures, 2017. **134**: p. 125-137.

[6] Hewes Jt and M.J.N. Priestley, *Seismic design and performance of precast concrete segmental bridge columns*. 2002, University of California: San Diego, CA.

[7] Chang Kc, Loh Ch, Chiu Hs, Hwang Js, Cheng Cb and Wang Jc, *Seismic behavior of precast segmental bridge columns and design methodology for applications in Taiwan.* Area National Expressway Engineering Bureau, 2002.

[8] Ou Yc, Chiewanichakorn M, Aref Aj and Lee Gc, *Seismic performance of segmental precast unbonded posttensioned concrete bridge columns.* Journal of Structural Engineering, 2007. **133**: p. 1636-1647.

[9] Chou Cc and Chen Yc, *Cyclic tests of post-tensioned precast CFT segmental bridge columns with unonded strands.* Earthquake Engineering and Structural Dynamics, 2006. **35**: p. 159-175.

[10] Marriott D, Pampanin S and Palermo A, *Quasi-stastic and pseudo-dynamic testing of unbonded post-tensioned rocking bridge piers with external replaceable dissipaters.* Earthquake Engineering and Structural Dynamics, 2009. **38**: p. 331-354.

[11] Eigawady Ma and Sha'lan A, *Seismic behavior of self-centering precast segmental bridge bents.* Journal of Bridge Engineering, 2010. **16**: p. 328-339.

[12] Motaref S, Saiidi Ms and Sanders Dh, *Experimental study of precast bridge columns with built-in elastomer.* Transport Res Rec: J Transport Res Board Bridge Eng, 2010. **3**: p. 109-116.

[13] Ou Yc, Tsai Ms, K.C. Chang and George F. Lee, *Cyclic behavior of precast segmental concrete*

bridge columns with high performance or conventional steel reinforcing bars as energy dissipation bars. Earthquake Engineering and Structural Dynamics, 2010. **39**: p. 1181-1198.

[14] Billington S and Yoon J, *Cyclic response of unbonded posttensioned precast columns with ductile fiber-reinforced concrete.* Journal of Bridge Engineering, 2004. **9**: p. 353-363.

[15] Chao Li, Hong Hao and Kaiming Bi, *Numerical study on the seismic performance of precast segmental concrete columns under cyclic loading.* Engineering Structures, 2017. **148**: p. 373-386.

[16] Ou Yc, Chiewanichakorn M, Aref Aj and Lee Gc, *Seismic performance of segmental precast unbonded postensioned concrete bridge columns.* Journal of Structural Engineering, 2007. **133**: p. 1636-1647.

[17] Tazarv M and Saiid M, *Low-damage precast columns for accelerated bridge construction in high seismic zones.* Journal of Bridge Engineering, 2015: p. 04015056.

[18] Lufeng Zhao, Kaiming Bi, Hong Hao and Xiaozhen Li, *Numerical studies on the seismic responses of bridge structures with precast segmental columns.* Engineering Structures, 2017. **151**: p. 568-583.

[19] Bipin Shrestha and Hong Hao, *Parametric study of seismic performance of superelastic shape memory alloy-reinforced bridge piers.* Structure and Infrastructure Engineering, 2015. **12**(9): p. 1076-1089.

[20] M. Saiid Saiidi, Melissa O'brien and Mahmoud Sadrossadat-Zadeh, *Cyclic response of concrete bridge columns using superelastic nitinol and bendable concrete.* ACI Structural Journal, 2009. **2**: p. 69-77.

[21] Wang Bin and Zhu Songye, *Seismic behavior of self-centering reinforced concrete wall enabled by superelastic shape memory alloy bars.* Bulletin of Earthquake Engineering, 2018. **16**: p. 479-502.

[22] Wang B., Zhu S.Y and Jiang H.J., *Earthquake resilient RC walls using shape memory alloy bars and replaceable energy dissipating devices.* Smart Material and Structures, 2019. **28**(6).

[23] Wang B. and Zhu S.Y., *Seismic behavior of self-centering reinforced concrete wall enabled by superelastic shape memory alloy bars.* Bulletin of Earthquake Engineering, 2018. **16**(1): p. 479-502.

[24] Shinozuka M, Chaudhuri S.R. and Mishra S.K., *Shape-memory-alloy supplemented lead rubber bearing for seismic isolation.* Probab. Eng. Mech., 2015. **130**(6): p. 34-45.

[25] M. S. Speicher, R. Desroches and R. T. Leon, *Experimental results of a NiTi shape memory alloy - based recentering beam-column connection.* Engineering Structures, 2011. **33**(9): p. 2448-2457.

[26] Zhu Songye and Zhang Yunfeng, *Seismic behavior of self-centering braced frame buildings with reusable hysteretic damping brace.* Earthquake Engineering and Structural Dynamics, 2007. **36**(10): p. 1329-1346.

[27] Casciati Sara, Faravelli Lucia and Vece Michele, *Investigation on the fatigue performance of Ni-Ti thin wires.* Structural Control and Health Monitoring, 2017. **24**(1): p. e1855.

[28] Ozbulut Osman E., Daghash Sherif and Sherif Muhammad M., *Shape Memory Alloy Cables for Structural Applications.* Journal of Materials in Civil Engineering, 2016. **28**(4).

[29] Wang Bing and Zhu Songye, *Cycle tension-compression behavior of superelastic shape memory*

alloy bars with buckling-restrained devices. Constructional Building Material, 2018. **186**: p. 103-113.

[30] Wang Bin, Zhu Songye, Chen Kaixin and Huang Jiahao, *Development of superelastic SMA angles as seismic-resistant self-centering devices.* Engineering Structures, 2020. **218**: p. 110836.

[31] Wang B., Zhu S.Y., Casciati F., Chen K.X. and Jiang H.J., *Cyclic behavior and deformation mechanism of superelastic SMA U-shaped dampers under in-plane and out-of-plane loadings.* Smart Material and Structures, 2021. **30**.

[32] Wang Bin, Minehiro Nishiyama, Zhu Songye, Masanori Tani and Jiang Huanjun, *Development of novel self-centering steel coupling beams without beam elongation for earthquake resilience.* Engineering Structures, 2021. **232**: p. 111827.

[33] Qiu Canxing and Zhu Songye, *Shake table test and numerical study of self-centering steel frame with SMA braces.* Earthquake Engineering and Structural Dynamics, 2017. **46**: p. 117-137.

[34] Casciati Fabio and Faravelli Lucia, *A passive control device with SMA components: from the prototype to the model.* Structural Control and Health Monitoring, 2009. **16**(7-8): p. 751-765.

[35] Casciati Sara, *SMA-based devices: insight across recent proposals toward civil engineering applications.* Smart Structures and Systems, 2019. **24**(1): p. 111-125.

[36] Qiu C.X., *Seismic-resisting self-centering structures with superelastic shape memory alloy*. 2016, Hong Kong Polytechnic University.

[37] Wang Bin and Zhu Songye, *Superelastic SMA U-shaped dampers with self-centering functions.* Smart Material and Structures, 2018. **27**: p. 055003.

[38] Junfeng Jia, Kaidi Zhang, Suiwen Wu, Yang Guo, Xiuli Du and Xu Wang, *Seismic performance of self-centering precast segmental bridge columns under different lateral loading directions.* Engineering Structures, 2020. **221**: p. 111037.

[39] Shao G, Jiang L and Chouw N, *Experimental investigations of the seismic performance of bridge piers with rounded rectangular cross sections.* Earthquake Structure, 2014. **7**: p. 463-484.

[40] Lbrahim Ama, Wu Z, Fahmy Mfm and Kamal D, *Experimental study on cyclic response of concrete bridge columns reinforced by steel and basalt FRP reinforcements.* J Compos Constr, 2015. **20**: p. 04015062.

[41] Cao Xy, Wu G and Ju J W W, *Seismic performance improvement of existing RCFs using external PT-PBSPC frame sub-structures: Experimental verification and numerical investigation.* Journal of Building Engineering, 2021: p. 103649.

[42] Jia-Jun Fang, Wu Gang, Feng Dc, Yi-Hua and Yong Lu, *Seismic performance of a novel self-sustaining beam-bolumn connection for precast concrete moment-resisting frames.* Engineering Structures, 2020. **222**(11): p. 111096.

[43] Cao Xy, Feng D C and Wang Z, *Parametric investigation of the assembled bolt-connected buckling-restrained brace and performance evaluation of its application into structural retrofit.* Journal of Building Engineering, 2022: p. 103988.

[44] Japan Road Association (Jra), *Design specifications for highway bridges, Part V, Seismic design*. 2012.

[45] American Concrete Institute (Aci), *Acceptance Criteria for Special Unbonded Post-Tensioned Precast Structural Walls Based on Validation Testing and Commentary*. 2019: Farmington Hills.

[46] Ministry of Housing and Urban-Rural Development of the People's Republic Of China, *Code for*

seismic design of buildings. 2010, China Architecture & Building Press: Beijing.

[47] Ali Davaran, Thierry Beland and Robert Tremblay, *Elastic-Plastic Analysis of Bolted Angles Usable in Steel Frame Connections.* Journal of Structural Engineering, 2019. **145**(7).

[48] Chen Zhi-Peng, Zhu Songye, Yu Haoran and Wang Bin, *Development of novel SMA-based D-type self-centering eccentrically braced frames.* Engineering Structures, 2022. **260**: p. 114228.

[49] Xihong Zhang, Hong Hao, Chao Li and Tin Van Do, *Experimental study on the behavior of precast segmental column with domed shear key and unbonded post-tensioning tendon under impact loading.* Engineering Structures, 2018. **173**: p. 589-605.